CLINICAL OBSTETRICS AND GYNECOLOGY
Volume 63, Number 1, 109–119

Characterization of a TP53 *Somatic Variant of Unknown Function From an Ovarian Cancer Patient Using Organoid Culture and Computational Modeling*

JIANLING BI, PhD,* KRISTINA W. THIEL, PhD,* JACOB M. LITMAN, PhD,† YUPING ZHANG, MS,* ERIC J. DEVOR, PhD,*‡ ANDREEA M. NEWTSON, MD,* MICHAEL J. SCHNIEDERS, PhD,§‖ JESUS GONZALEZ BOSQUET, MD, PhD,* and KIMBERLY K. LESLIE, MD*‡

*Departments of *Obstetrics and Gynecology; ‖Biochemistry; §Biomedical Engineering; ‡Holden Comprehensive Cancer Center, University of Iowa, Iowa City, Iowa; and †Department of Biomedical Engineering, Cockrell School of Engineering, University of Texas at Austin, Austin, Texas*

Correspondence: Kimberly K. Leslie, MD, Jennifer Niebyl Chair, and DEO, Department of Obstetrics and Gynecology, University of Iowa, 31140 PFP, 200 Hawkins Drive, Iowa City, IA. E-mail: kimberly-leslie@uiowa.edu

J.B. and K.W.T. contributed equally.

Supported in part by the National Institutes of Health (R01CA099908 to K.K.L. and R01CA184101 to K.K.L.), National Science Foundation (CHE-1751688 to M.J.S.) and the University of Texas at Austin (Donald D. Harrington Faculty Fellowship to M.J.S.). The funders had no role in study design, data interpretation or decision to publish.

K.W.T.: is a cofounder of Immortagen Inc., and holds an equity stake in the Company. The remaining authors declare that they have nothing to disclose.

Abstract: In our proof-of-concept study of 1 patient with stage IIIC carcinosarcoma of the ovary, we discovered a rare mutation in the tumor suppressor, *TP53*, that results in the deletion of N131. Immunofluorescence imaging of the organoid culture revealed hyperstaining of p53 protein. Computational modeling suggests this residue is important for maintaining protein conformation. Drug screening identified the combination of a proteasome inhibitor with a histone deacetylase inhibitor as the most effective treatment. These data provide evidence for the successful culture of a patient tumor and analysis of drug response ex vivo.
Key words: ovarian cancer, p53, organoid culture, drug screen

Introduction

Epithelial ovarian cancer is the most deadly of the gynecologic malignancies[1] and the fifth leading cause of cancer-related death among women.[2] Treatment normally consists of surgical debulking followed by 6 cycles of platinum and taxane-based chemotherapy. However, the asymptomatic nature of the disease partnered with a high rate of recurrence results in a long-term survival rate of only 30%.[2,3] For these women, the evaluation of new agents must be a priority.

The classic model systems used to evaluate new therapeutic agents for ovarian cancer include immortalized cell lines, patient-derived xenograft models, syngeneic and genetically engineered mouse models, and short-term culture of primary tumor cells. Each of these methods has caveats. For example, many immortalized cell lines do not faithfully represent human disease,[4] with significant genetic drift associated with extended culture. Patient-derived xenograft models retain many of the phenotypic and genetic features of the primary tumor. However, since these models must be created in immunocompromised mice to avoid host versus graft responses, it is not possible to study the impact of the immune system on tumor response. Although syngeneic mice and genetically engineered mouse models do allow for the evaluation of immunomodulatory agents, these models deviate from human tumor features. The short-term culture of primary tumor cells has been attempted for decades, but recent success is attributed to optimized growth media and the use of Matrigel to provide the structural support for 3-dimensional growth.

First developed for colorectal cancer in 2011 by Clevers and colleagues in the Netherlands,[5] patient-derived organoid culture is an emerging and novel technology to model cancer. The organoid culture technology includes a cocktail of growth factors to recreate the niche of tissue homeostasis ex vivo. The general protocol includes enzymatic digestion of tumor tissue into single cells, followed by embedding the cells into Matrigel and culture with specific medium optimized for the cancer type.

A handful of studies in several cancer types have established that organoids can recapitulate both histological and genomic features of the pertinent lesion from which they were derived. Very recent work by the Soragni laboratory reported a method for high throughput drug screening using organoid cultures.[6] Importantly, Vlachogiannis et al,[7] have reported a positive predictive value (predicting that a particular drug works) of 88% and a negative predictive value (predicting that a particular drug does not work) of 100% when comparing organoid sensitivity to the response of a patient with gastrointestinal cancer.

Herein we present proof-of-concept data that we can create an organoid model of ovarian cancer using cancer cells isolated from ascites fluid that was collected at the time of initial debulking.

Materials and Methods

HUMAN SUBJECTS

Human subjects studies were approved by the University of Iowa Institutional Review Board (IRB). Informed consent was obtained under IRB protocol #2018090807,

Molecular Genetic Study of Gynecologic Specimens and Data Repository.

SPECIMEN COLLECTION

The patient was taken to the operating room, where a midline vertical incision was made. Two hundred milliliters of ascites was collected in a sterile container and placed in a biohazard bag. This was then immediately handed off to lab personnel for processing.

ISOLATION OF TUMOR CELLS FROM ASCITES FLUID

On arrival, the ascites fluid was transferred from the vacuum container to 50 mL tubes. Next, 5 mL of 50% vol/vol Percoll was aliquoted into each of 16 to 20 15 mL conical centrifuge tubes. Five milliliters of ascites was carefully layered onto the 50% vol/vol Percoll cushion in each tube, followed by centrifugation at 1200*g* for 20 minutes at 4°C using a swinging bucket rotor. Erythrocytes pellet at the bottom of the tubes, while the desired ovarian cancer cells are at the interphase between the ascites fluid and Percoll. Using a 5 mL pipet, cancer cells were carefully withdrawn from the interphase fraction and transferred to a new 15 mL conical tube. To remove residual red blood cells, 2 mL of blood cell lysis buffer was added.

RNA PURIFICATION

Ascites cells were collected and total cellular RNA was purified using the mirVana RNA Purification Kit following manufacturer's (Thermo Fisher) recommendations. RNA yield and purity were determined on an Agilent Model 2100 Bioanalyzer. Sufficient yield was obtained with an RNA Integrity Number (RIN) >9.0 to proceed with RNA sequencing.

TP53 SEQUENCING

Sanger sequencing of *TP53* was carried out using 100 ng of purified cellular RNA. This RNA was reverse transcribed in the presence of SuperScript III reverse transcriptase (Thermo Fisher). The resulting cDNA was then amplified using the *TP53* primers p53mRNAfor: AGCCGCAGTCAGATCCTA and p53mRNArev: GA AGTCCTGGGTGCTTCTG. The 1302 bp amplicon was prepared for Sanger sequencing using the QIAquick PCR Purification Kit following manufacturer's (Qiagen) recommendations. Using the PCR primers as sequencing primers, the mRNA amplicon was sequenced in both directions on an Applied Biosystems Model 3730XL platform and aligned against the mRNA sequence NM_000546.

COMPUTATIONAL MODELING OF p53

Simulated annealing was used to generate a plausible structure of the S2-S2′ region (residues K120-Q136) with the delN131 (ΔN131) mutation. The same protocol was also applied to the WT protein to ensure a fair comparison. The 3KMD crystal structure[8] was used as our baseline. Zinc-coordinating cysteines 176, 238, and 242 were deprotonated, and the zinc-coordinating H179 was deprotonated at the δ nitrogen. Then, H193 and H214 were deprotonated at the δ and ε nitrogens, respectively, as they form a buried π-stack, have a depressed pKa predicted by PROPKA,[9,10] and were assigned as neutral by Pradhan et al.[11] Using Force Field X (FFX),[12] the structure was re-refined with the polarizable atomic multipole AMOEBA 2018 protein force field.[13–15]

Subsequently, chain A was solvated in a 75.951 Å water box with a total of 13,168 water molecules (including crystal waters) with 100 mM NaCl (27 copies) and 8 additional chloride ions to neutralize the system. This was then minimized using the limited memory Broyden-Fletcher-Goldfarb-Shanno algorithm[16,17] (LBFGS) algorithm to a convergence criterion of 0.1 kcal/(mol×Angstrom) using FFX-OpenMM.[18] This was then equilibrated for 2 nsec with 40 kcal/(mol×Angstrom) harmonic heavy atom restraints at 298.15K. Asparagine

131 was then removed from the structure, and the structure re-minimized to the same convergence criterion while constraining all atoms outside the range Y35 to F43 to the equilibrated structure. Both the WT equilibrated structure and the ΔN131 structure were then annealed, initially at 1000K for 500 psec, then 200 psec each of 800K, 600K, 400K, 300K, 250K, 200K, 150K, and 100K, finishing with 500 psec of dynamics at 50K. During this annealing, protein-heavy atoms and the zinc ion outside the range K120 to Q136 were restrained to the equilibrated structure with 100 kcal/(mol×Angstrom) harmonic restraints.

All dynamics were performed in the NVT ensemble using FFX-OpenMM on NVIDIA Titan V accelerators. The NVT ensemble was maintained with an Andersen thermostat[19] with a collision frequency of 91/psec and a RESPA multiple timestep integrator[20,21] with 0.5 fsec inner timesteps and 2 fsec outer timesteps. The van der Waals interactions were smoothly switched off between 10.8 and 12.0 Å. The Particle Mesh Ewald algorithm[12,22] was used for long-range electrostatics, with an Ewald coefficient of 0.545, a 7.0 Å real-space cutoff, fifth-order B-splines, and a 96×96×96 grid. Extrapolated perturbation theory[23] was used for mutual polarization.

GENERATION OF ORGANOID MODEL USING CANCER CELLS FROM ASCITES FLUID

Cancer cell pellets were suspended in AdDE+++ medium and filtered with a 40 μm cell strainer. After centrifugation at 2500 rpm for 5 minutes, the cell pellet was suspended with cool Matrigel (1×10^5 to 5×10^5 cells/mL) and mixed well with a cold tip. Spheroids (20 μL in Matrigel) were transferred to 1 well of a 96-well plate; the liquid Matrigel was allowed to solidify by placing the plate in a 37°C incubator for 15 minutes. Next, 200 μl AdDE+++ media was added to the top of the Matrigel. Media was changed every 6 to 7 days and organoids were passaged every 2 to 4 weeks.

The AdDE+++ medium recipe (200 mL)

AdDE+++ (advanced DMEM/F12: 1x glutamax, 10 mM HEPES)	191 mL
Noggin (100 μg/mL)	200 μL
Rspo1 (25 μg/mL)	2 mL
B27 (50×)	4 mL
N-Acetylcysteine (500 mM)	0.5 mL
Primocin	0.4 mL
Nicotinamide (1 M)	2 mL
A83-01 (5 mM)	20 μL
FGF 10 (100 μg/mL)	20 μL
Heregulin β-1 (75 μg/mL)	100 μL
Y27632 (100 mM)	10 μL
EGF (500 μg/mL)	2 μL
Forskolin (10 mM)	200 μL
Hydrocortisone (250 μg/mL)	400 μL
β-Estradiol (100 μM)	200 μL
Total	200 mL

IMMUNOFLUORESCENCE IMAGING

Organoids were grown on glass coverslips and treated with indicated reagents. After fixation with 2% paraformaldehyde and permeabilization with 1% Triton X-100, cells were labeled with a p53 antibody (sc-126; Santa Cruz) and PAX8 antibody (10336-1-AP; Proteintech) followed by incubation with Alexa Fluor-555 (for p53) or Alexa Fluor-488 (for PAX8)-conjugated secondary antibody. Images were visualized by fluorescence microscopy and acquired with an Olympus BX51 camera at ×63 magnification.

HEMATOXYLIN AND EOSIN (H&E) STAINING

Formalin-fixed, paraffin-embedded organoids section were stained using H&E program 8 from Central Microscopy facility, the University of Iowa, dehydrated using 3 washes of ethanol and xylene, and mounted with coverslips.

DRUG SCREENING

The viability of the tumor organoids following drug treatment was determined by the CellTiter-Glo 3D cell viability

assay (Promega, Madison, WI). In brief, tumor cells were suspended in AdDE+++ medium with 20% Matrigel and seeded at a density of 3000 cells/well (200 μL/well) in an ultra-low attachment 96-well U-bottom white plate. After 24 hours, cells were then exposed to cisplatin (5 μM), carboplatin (5 μM), paclitaxel (10 nM), bevacizumab (1 μM), AZD1775 (125 nM), bortezomib (10 nM), belinostat (1 μM) or olaparib (2 μM) for 72 hours at 37°C. At the end of incubation, an equal volume of CellTiter-Glo 3D reagent was added to each well and incubated for 25 minutes at room temperature. The luminescence was measured using the Gen5 Microplate Reader (BioTek, VT). All the tests were conducted in triplicate and data normalized to untreated control (set at 100% viability).

Results

PATIENT CHARACTERISTICS

This proof-of-concept study was performed using tumor cells collected from the ascites fluid of a patient undergoing primary cytoreductive surgery. The patient is a 77-year-old woman who presented with abdominal bloating and discomfort. Her imaging was concerning for advanced stage gynecologic malignancy, and she was recommended for primary cytoreductive surgery. During surgery, she was found to have bilateral adnexal masses obscuring the gynecologic organs and obliterating the rectovaginal space, as well as an omental cake, tumor plaquing of the right hemidiaphragm, and miliary disease along the small bowel mesentery and descending colon. She underwent an optimal tumor cytoreduction consisting of a total abdominal hysterectomy with bilateral salpingo-oophorectomy with en block rectosigmoid resection with end to end anastomosis, infragastric and infracolic omentectomy, diaphragmatic peritonectomy with diaphragm resection and primary repair, and appendectomy. Her postoperative course was complicated by a bowel leak from her rectosigmoid re-anastomosis, which required a return to the operating room for an abdominal washout and diverting loop colostomy. She recovered in the intensive care unit on broad-spectrum antibiotics and pressors, transferred to the general care unit, and finally discharged on a postoperative day 36 from her initial surgery. The patient went home on enteral nutrition based on her continued poor oral intake. Final pathology was stage IIIC carcinosarcoma of the ovary. She was recommended to complete 6 cycles of carboplatin and paclitaxel but started with single-agent carboplatin until her performance status improves.

GENERATION OF ORGANOID EX VIVO MODEL OF PATIENT TUMOR CELLS

Cancer cells were isolated from the ascites fluid and used to generate an organoid model of the patient's disease as described in *Material and Methods*. We first performed pathologic analysis of the organoids using H&E staining and found that cells form sphere-like structures (Fig. 1A). Immunofluorescent staining with protein biomarkers paired box gene 8 (PAX8) and p53 confirmed that the tumor is ovarian in origin (Figs. 1B, C). Interestingly, p53 was highly expressed in the tumor organoids by both immunofluorescence and immunohistochemistry (Figs. 1C, D).

IDENTIFICATION OF A TP53 VARIANT OF UNKNOWN FUNCTION

We next examined the *TP53* status of the tumor since *TP53* is commonly mutated in carcinosarcomas of the ovary[24] and was overexpressed in the tumor organoid (Figs. 1C, D). Mutations in *TP53* can be binned in a variety of ways, but the most commonly used nomenclature is to bin the mutations into 1 of 3 simplistic functional classes: (1) truncating, frameshift or splice site loss-of-function mutations that mainly result in a p53-null state, (2) missense

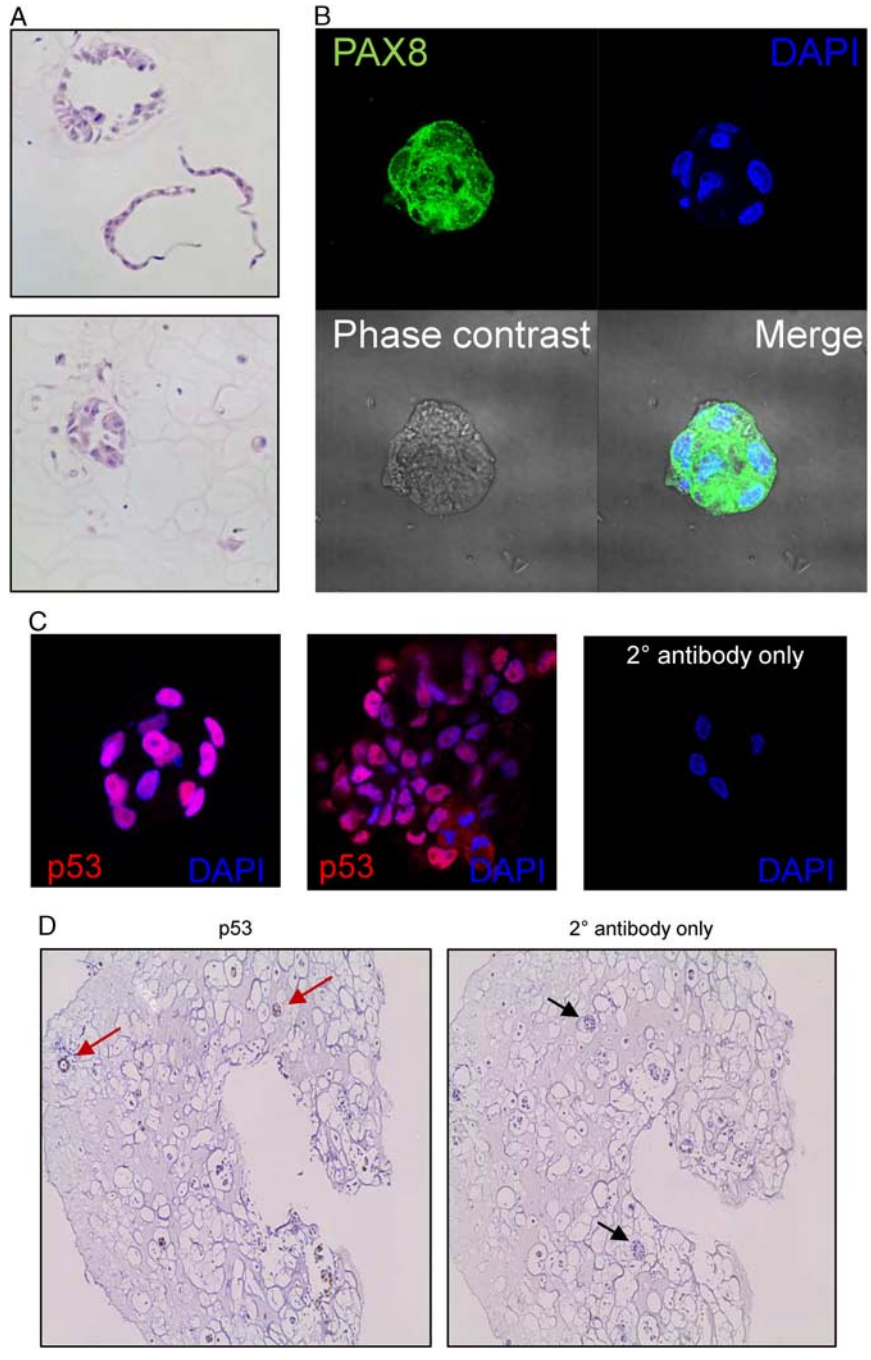

FIGURE 1. Characterization of organoid culture. A, Hematoxylin and eosin staining of paraffin-embedded section. B and C, Immunofluorescent imaging for PAX8 (B) or p53 (C). Nuclei were counterstained with DAPI. D, Immunohistochemistry for p53. Arrows indicate organoids. Other structures are Matrigel. full color online

mutations that often result in gain-of-oncogenic function (GOF), and (3) synonymous/silent mutations that are wild-type (WT) equivalent. Of the missense mutations, ~8 mutations are canonically recognized as "GOF" based on a variety of functional studies[25]: P151S, Y163C, R175H, L194R, Y220C, R248Q, R248W, R273C, R273H, R273L, R282W.

The aligned mRNA sequence from the patient-derived tumor cells revealed a single mutation event in the *TP53* gene. A deletion of 3 bases (AAG) in Exon 5 resulted in an in-frame deletion of asparagine residue 131 (ΔN131).

In a previous analysis of The Cancer Genome Atlas (TCGA) dataset for ovarian cancer, we found that nearly one half of tumors harbor missense mutations in *TP53* that are not classic GOF mutations.[26] We term these missense mutations "somatic variants of unknown function" because there is not a standardized nomenclature for them. The often-used terminology "variants of unknown significance" refers to germline variants with unclear risk of disease, which is not the case when a patient already has cancer. Therefore, we characterize the ΔN131 mutation as a somatic variants of unknown function.

COMPUTATIONAL MODELING TO PREDICT THE FUNCTIONAL IMPACT OF ΔN131 MUTATION

Since the ΔN131 variant is not a traditional loss-of-function or GOF mutation, our next objective was to model the functional consequences of the deletion of N131. p53 is a well-characterized transcription factor with tumor suppressor activities. p53 GOF mutants are typically broadly divided into 2 categories: (1) *contact mutants* that have lost the ability to bind DNA (eg, R273H, R248Q/W); and (2) *structural mutants* that alter the conformation of the protein (eg, R175H, Y220C).[27] Our prior TCGA analysis of ovarian tumors demonstrated a high frequency in *TP53* mutations in the DNA-binding domain.[26]

In the p53 protein structure, asparagine 131 is part of a β-turn between the S2 and S2′ β-sheet segments[28] (Fig. 2A). The S2-S2′ region lies in between sheet S10 and helix H2, and likely holds them together. The H2 helix is notable for directly contacting DNA, while the S10 helix is part of the main β-sandwich structure. As such, it is thought that without the S2 and S2′ β-sheet, the H2 helix may become separated from the rest of the DBD and impact binding affinity. Numerous specific interactions hold the S10-S2′-S2-H2 bundle together (Table 1). In particular, L130 forms a hydrophobic contact with helix H2 (Fig. 2B), and it is almost certain that hydrophobic effects are central to protein folding. To confirm this, we used a global structural

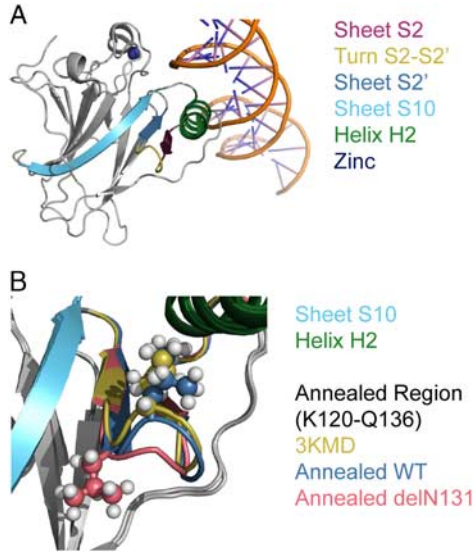

FIGURE 2. Cartoon representations of p53 (PDB ID: 3KMD). A, Zoomed out view of chain A and the DNA; protein chains B-D are excluded for clarity. B, Overlay of 3KMD chain A with optimized structures from simulated annealing of residues K120 to Q136. The side chain of L130 is shown in ball-and-stick representation. When N131 is deleted, L130 shifts downwards and fails to contact helix H2. full color online

TABLE 1. Key Interactions Formed by Residues in S2, S2′, and the Intervening Turn (T2-T2′) in p53

N-terminal Site	Location	C-terminal Site	Location	Nature of Interaction
C124	S2	C135	S2′	Potential disulfide bond site
T125	S2	F134	S2′	β-sheet H-bond
T125	S2	R282	H2	Side chain H-bond
T125	S2	Y126	S2	Side chain-main chain H-bond
Y126	S2	N131	S2′	Side chain H-bond
S127	S2	L130	T2-2′	Main chain H-bond
S127	S2	L130	T2-2′	Side chain-main chain H-bond
S127	S2	N131	T2-2′	Main chain H-bond
S127	S2	K132	S2′	β-sheet H-bond
S127	S2	K132	S2′	β-sheet H-bond
S127	S2	E286	H2	Side chain H-bond
P128	S2	N131	T2-2′	Main chain H-bond
L130	T2-2′	L289	H2	Hydrophobic contact
N131	T2-2′	S269	S10	Side chain-main chain H-bond
N131	T2-2′	E271	S10	β-sheet H-bond
K132	S2′	E271	S10	Salt bridge
K132	S2′	E271	S10	β-sheet H-bond
M133	S2′	E271	S10	β-sheet H-bond
M133	S2′	R273	S10	β-sheet H-bond
F134	S2′	R282	H2	Hydrophobic contact
C135	S2′	R273	S10	β-sheet H-bond

p53 structures used for this analysis: 3KMD, 2FEJ, 3IGK, 5BUA, 5LGY, 5MCT, and 6FJ5. The major discrepancy between structures in this region is that H2 did not appear to be as well-ordered in many members of the 2FEJ NMR ensemble.

optimization method called simulated annealing in the FFX program[29] to find low-energy conformations of the S2-S2′ region (defined as residues K120-Q136). Although the WT structure maintained the L130-H2 interaction throughout the simulation, even at substantially elevated temperatures (Fig. 2B, dark blue), the ΔN131 mutant showed the L130 movement away from H2 within 60 psec and never returned to an H2-interacting conformation (Fig. 2B, red). This suggests that strain introduced in the β-turn by ΔN131 results in loss of key stabilizing interactions in the S10-S2′-S2-H2 region, including a hydrophobic contact made by L130.

DRUG SCREENING DEMONSTRATES SENSITIVITY OF TUMOR ORGANOIDS TO A RANGE OF AGENTS

To demonstrate the ovarian cancer organoids culture platform is suitable for drug screening, tumor organoids were treated with indicated drugs for 72 hours then the cell viability assay was performed with CellTiter-Glo 3D assay (Fig. 3). The results showed that this patient's organoids were most sensitive to the combination of bortezomib and belinostat, and also quite sensitive to bortezomib, paclitaxel, and AZD1775 alone, but not sensitive to bevacizumab or olaparib. It is also important to note that the tumor organoid was relatively sensitive to the combination of carboplatin and paclitaxel, the standard front-line treatment for carcinosarcoma patients.

Discussion

To make meaningful predictions regarding how each patient is likely to respond to therapy, it is critical to have a reasonable understanding of the function of each p53 mutant. Several algorithms have been developed to predict if mutations are

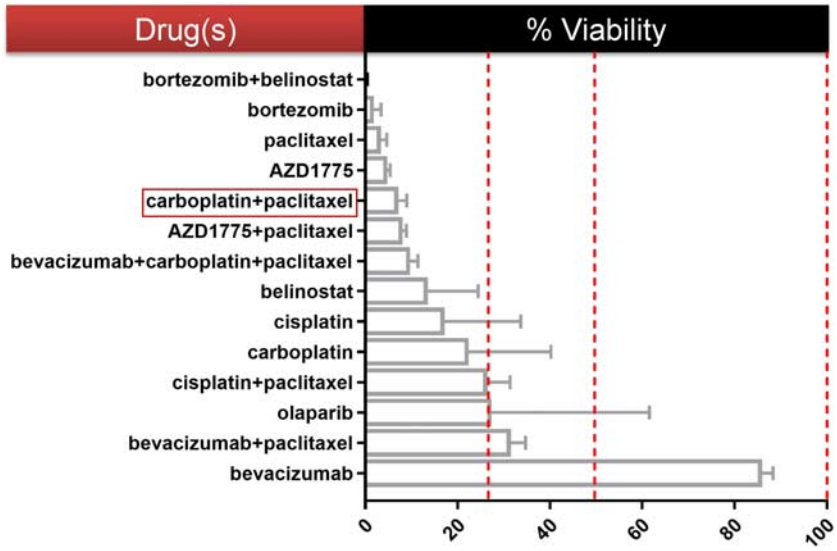

FIGURE 3. Drug screening using patient organoid. As noted with the red box, carboplatin+paclitaxel is the standard front-line treatment for ovarian carcinosarcoma. full color online

deleterious from the perspective of protein structure,[30] but they do not predict how the mutants affect protein function. Rather, these predictions are binary pathogenic versus benign predictions. Missense mutations may be difficult to characterize based upon predictions of structure alone, and overexpression at the protein level is not always an indicator of oncogenic GOF activity.

The ΔN131 mutant results from an in-frame deletion of nucleotides AAC at positions c.391-c.393 of the *TP53* gene (GRCh38 chromosome 17 coordinates 7675175-7675173). This mutation has been reported independently in a Wilms tumor patient,[31] a serous ovarian cancer patient,[32] a patient with neuroendocrine small cell carcinoma of the uterine cervix,[33] and a patient with adenocarcinoma of the stomach.[34] In the first 2 studies,[31,32] the presence of this mutation was marked by elevated production and accumulation of p53 protein. Herein we document that p53 expression is high in the organoid culture that harbors the ΔN131 p53 mutant protein. However, additional studies are necessary to determine the mechanism of hyperexpression, as well as functional consequences. We speculate that this indel results in a GOF-type p53 protein.

The p53 molecule contains a Zn^{++} pocket in the DNA-binding domain formed by the residues C176 and H179 in the L2 loop and C238 and C242 in the L3 loop. There is evidence that disruption of optimal folding of p53 will impact retention of the Zn^{++} and lead to significant loss of DNA-binding specificity.[35] Numerous biochemical and cellular studies have confirmed that proper binding and retention of the Zn^{++} divalent cation is crucial to p53 function and that even minor alterations can significantly disrupt that function.[36] Our analysis of the structural impact of the N131 deletion suggests that this indel results in loss of Zn^{++} binding and therefore DNA binding.

Our drug screening results may provide insights for doctors in further treatment for this patient in the clinic. GOF p53 is frequently hyper-stabilized by Hsp90, and we and others have found that strategies that promote Hsp90 acetylation (ie, histone deacetylase inhibitor) sensitize cells with

GOF p53 to chemotherapy.[37,38] Our recent study in gynecologic cancer cells with 2 different *TP53* GOF mutations indicates that greater cell toxicity can be achieved by the addition of a histone deacetylase inhibitor to the backbone treatment of a proteasome inhibitor.[39] Our long-term vision is to deploy this platform to determine drug sensitivities of primary specimens, which can offer actionable information to help tailor therapy to individual cancer patients.

References

1. Cancer Facts and Figures 2018; 2018. Available at: www.cancer.org/content/dam/cancer-org/research/cancer-facts-and-statistics/annual-cancer-facts-and-figures/2018/cancer-facts-and-figures-2018.pdf. Accessed June 26, 2018.
2. Siegel R, Naishadham D, Jemal A. Cancer statistics, 2013. *CA Cancer J Clin*. 2013;63:11–30.
3. Cannistra SA. Cancer of the ovary. *N Engl J Med*. 2004;351:2519–2529.
4. Domcke S, Sinha R, Levine DA, et al. Evaluating cell lines as tumour models by comparison of genomic profiles. *Nat Commun*. 2013;4:2126.
5. Sato T, Stange DE, Ferrante M, et al. Long-term expansion of epithelial organoids from human colon, adenoma, adenocarcinoma, and Barrett's epithelium. *Gastroenterology*. 2011;141:1762–1772.
6. Phan N, Hong JJ, Tofig B, et al. A simple high-throughput approach identifies actionable drug sensitivities in patient-derived tumor organoids. *Commun Biol*. 2019;2:78.
7. Vlachogiannis G, Hedayat S, Vatsiou A, et al. Patient-derived organoids model treatment response of metastatic gastrointestinal cancers. *Science*. 2018;359:920–926.
8. Chen Y, Dey R, Chen L. Crystal structure of the p53 core domain bound to a full consensus site as a self-assembled tetramer. *Structure*. 2010;18:246–256.
9. Olsson MH, Søndergaard CR, Rostkowski M, et al. PROPKA3: consistent treatment of internal and surface residues in empirical pKa predictions. *J Chem Theory Comput*. 2011;7:525–537.
10. Søndergaard CR, Olsson MH, Rostkowski M, et al. Improved treatment of ligands and coupling effects in empirical calculation and rationalization of pKa values. *J Chem Theory Comput*. 2011;7:2284–2295.
11. Pradhan MR, Siau JW, Kannan S, et al. Simulations of mutant p53 DNA binding domains reveal a novel druggable pocket. *Nucleic Acids Res*. 2019;47:1637–1652.
12. Schnieders MJ, Fenn TD, Pande VS. Polarizable atomic multipole X-ray refinement: particle mesh Ewald electrostatics for macromolecular crystals. *J Chem Theory Comput*. 2011;7:1141–1156.
13. Piquemal JP, Perera L, Cisneros GA, et al. Towards accurate solvation dynamics of divalent cations in water using the polarizable amoeba force field: from energetics to structure. *J Chem Phys*. 2006;125:054511.
14. Shi Y, Xia Z, Zhang J, et al. Polarizable atomic multipole-based AMOEBA force field for proteins. *J Chem Theory Comput*. 2013;9:4046–4063.
15. Jing Z, Qi R, Liu C, et al. Study of interactions between metal ions and protein model compounds by energy decomposition analyses and the AMOEBA force field. *J Chem Phys*. 2017;147:161733.
16. Liu DC, Nocedal J. On the limited memory BFGS method for large-scale optimization. *Math Program*. 1989;45:503–528.
17. Byrd RH, Lu PH, Nocedal J, et al. A limited memory algorithm for bound constrained optimization. *SIAM J Sci Comput*. 1995;16:1190–1208.
18. Eastman P, Swails J, Chodera JD, et al. OpenMM 7: rapid development of high performance algorithms for molecular dynamics. *PLoS Comput Biol*. 2017;13:17.
19. Andersen HC. Molecular dynamics simulations at constant pressure and/or temperature. *J Chem Phys*. 1980;72:2384–2393.
20. Humphreys DD, Friesner RA, Berne BJ. A multiple-time-step molecular dynamics algorithm for macromolecules. *J Phys Chem*. 1994;98:6885–6892.
21. Qian X, Schlick T. Efficient multiple-time-step integrators with distance-based force splitting for particle-mesh-Ewald molecular dynamics simulations. *J Chem Phys*. 2002;116:5971–5983.
22. Darden T, York D, Pedersen L. Particle mesh Ewald: an N * log(N) method for Ewald sums in large systems. *J Chem Phys*. 1993;98:10089–10092.
23. Simmonett AC, Pickard FC IV, Shao Y, et al. Efficient treatment of induced dipoles. *J Chem Phys*. 2015;143:074115.
24. Zhao S, Bellone S, Lopez S, et al. Mutational landscape of uterine and ovarian carcinosarcomas implicates histone genes in epithelial-mesenchymal transition. *Proc Natl Acad Sci USA*. 2016;113:12238–12243.
25. Brachova P, Thiel KW, Leslie KK. The consequence of oncomorphic TP53 mutations in ovarian cancer. *Int J Mol Sci*. 2013;14:19257–19275.
26. Brachova P, Mueting SR, Carlson MJ, et al. TP53 oncomorphic mutations predict resistance to platinum and taxane-based standard chemotherapy in patients diagnosed with advanced serous ovarian carcinoma. *Int J Oncol*. 2015;46:607–618.
27. Mello SS, Attardi LD. Not all p53 gain-of-function mutants are created equal. *Cell Death Differ*. 2013;20:855–857.

28. Joerger AC, Fersht AR. Structural biology of the tumor suppressor p53. *Annu Rev Biochem*. 2008;77:557–582.
29. Tollefson MR, Litman JM, Qi G, et al. Structural insights into hearing loss genetics from polarizable protein repacking. *Biophys J*. 2019;117:602–612.
30. Dong C, Wei P, Jian X, et al. Comparison and integration of deleteriousness prediction methods for nonsynonymous SNVs in whole exome sequencing studies. *Hum Mol Genet*. 2015;24:2125–2137.
31. Wegert J, Vokuhl C, Ziegler B, et al. TP53 alterations in Wilms tumour represent progression events with strong intratumour heterogeneity that are closely linked but not limited to anaplasia. *J Pathol Clin Res*. 2017;3:234–248.
32. Devor EJ, Gonzalez-Bosquet J, Warrier A, et al. p53 mutation status is a primary determinant of placenta-specific protein 1 expression in serous ovarian cancers. *Int J Oncol*. 2017;50:1721–1728.
33. Saga Y, Suzuki M, Tamura N, et al. Establishment and characterization of a new cell line (SKS) from neuroendocrine small cell carcinoma of the uterine cervix and its chemosensitivity. *Oncology*. 2001;60:367–372.
34. TCGA Data Portal. Available at: https://tcga-data.nci.nih.gov/tcga/. Accessed November 25, 2019.
35. Loh SN. The missing zinc: p53 misfolding and cancer. *Metallomics*. 2010;2:442–449.
36. Yu X, Blanden AR, Narayanan S, et al. Small molecule restoration of wildtype structure and function of mutant p53 using a novel zinc-metallochaperone based mechanism. *Oncotarget*. 2014;5:8879–8892.
37. Lin K, Rockliffe N, Johnson GG, et al. Hsp90 inhibition has opposing effects on wild-type and mutant p53 and induces p21 expression and cytotoxicity irrespective of p53/ATM status in chronic lymphocytic leukaemia cells. *Oncogene*. 2008;27:2445–2455.
38. Meng X, Dizon DS, Yang S, et al. Strategies for molecularly enhanced chemotherapy to achieve synthetic lethality in endometrial tumors with mutant p53. *Obstet Gynecol Int*. 2013;2013:828165.
39. Meng X, Yang S, Li Y, et al. Combination of proteasome and histone deacetylase inhibitors overcomes the impact of gain-of-function p53 mutations. *Dis Markers*. 2018;2018:3810108.